

# Fast Unveiling of $T_{\max}$ in GaN HEMT Devices via the Electrical Measurement-Assisted Two-Heat Source Model

Hasan Kocer<sup>1</sup>, Yilmaz Durna<sup>1</sup>, Burak Gunes<sup>1</sup>, Gizem Tendurus, Bayram Butun<sup>1</sup>, and Ekmel Ozbay<sup>1</sup>

**Abstract**—Gallium nitride (GaN) high-electron-mobility transistor (HEMT) devices, which have wide application potential from power amplifiers to satellite, need to be thoroughly examined in terms of reliability in order to benefit the superior intrinsic properties of the device. The most critical parameter in the device reliability is the hotspot, or  $T_{\max}$ , which occurs somewhere on the subsurface and along the channel of the GaN HEMT, which is optically inaccessible due to optical path disability. Therefore, the  $T_{\max}$  value is underestimated in optical measurements, such as the thermographic IR and Raman methods. With 3-D electrothermal simulations,  $T_{\max}$  is obtained close to reality, but it requires a huge computation load and the complex modeling of semiconductor device physics. In 2-D or 3-D thermal simulations that do not use electrothermal simulations, since the self-heating is mostly modeled with a single heat source, neither the correct  $T_{\max}$  value is obtained nor the effect of bias conditions is considered. To address the aforementioned shortcomings, a hybrid method is demonstrated, which exploits the electrical measurements of GaN HEMT, which RF and reliability engineers often and easily do. It is demonstrated that  $T_{\max}$  can be determined quickly and close to the electrothermal simulations in a GaN HEMT

device with a two-heat source method and finite element analysis (FEA) hybrid interaction with respect to various bias conditions. Moreover, the impact of the knee voltage is investigated with different knee-detection techniques. The proposed method provides GaN HEMT reliability engineers with an easy-to-implement alternative to reveal the hotspot location and the value.

**Index Terms**—Finite element analysis (FEA), high-electron-mobility transistors (HEMTs), thermal analysis.

## I. INTRODUCTION

GALLIUM nitride (GaN)-based high-electron-mobility transistors (HEMTs) have become increasingly attractive in recent years, both academically and commercially, due to their appealing advantages in applications such as high-performance radars, advanced satellite and space systems, emerging 5G communication, digital and quantum computing electronics, high-power amplifiers, and monolithic microwave integrated circuits (MMICs) [1]–[8]. The most salient advantages of GaN HEMTs [9]–[12] are: 1) ability to operate at high voltages due to the wide bandgap of the III–V material in the device architecture; 2) due to 2-D electron gas (2DEG) confinement at the heterointerface, superior electron transport characteristics (high electron mobility and saturation velocity), and the resulting high current capability; 3) ability to operate at high frequencies over 100 GHz; and 4) ability to work at high powers due to its high-voltage and high-current processing capability.

Self-heating, which occurs mostly in GaN HEMT devices operating at high power densities, is an important issue to manage, as it affects the device lifetime and reliability. The thermal power, called Joule or ohmic heating, is inevitably produced by the interaction of the electric field emerging from the nonzero operating output voltage and the nonzero current density passing through the device [13]. Depending on the amplitude and positional variation of the electric field and current density, the intensity and spatial variation of the thermal power may differ throughout the device channel and the nearby locations. If this excess heat is not removed to the heat sinking (cold) regions with appropriate thermal management and heat transfer methods, it will cause very high temperatures ( $>250\text{ }^{\circ}\text{C}$ ) inside the device. Fundamental transport parameters, such as electron mobility and saturation velocity, which impact the

Manuscript received January 14, 2022; revised March 21, 2022; accepted March 23, 2022. Date of publication April 7, 2022; date of current version April 22, 2022. This work was supported in part by Turkcell Technology within the framework of 5G and Beyond Joint Graduate Support Program coordinated by the Information and Communication Technologies Authority. The work of Burak Gunes was supported in part by Turkcell Technology within the framework of 5G and Beyond Joint Graduate Support Program coordinated by the Information and Communication Technologies Authority. The work of Ekmel Ozbay was supported in part by the Turkish Academy of Sciences. The review of this article was arranged by Editor S. Graham. (Corresponding author: Hasan Kocer.)

Hasan Kocer, Yilmaz Durna, and Bayram Butun are with the Nanotechnology Research Center (NANOTAM), Bilkent University, 06800 Ankara, Turkey (e-mail: hasan.kocer@bilkent.edu.tr; yilmaz.durna@bilkent.edu.tr; bbtn@bilkent.edu.tr).

Burak Gunes is with the Nanotechnology Research Center (NANOTAM), Department of Electrical and Electronics Engineering, Bilkent University, 06800 Ankara, Turkey, and also with Turkcell Technology, 34347 Istanbul, Turkey (e-mail: burakg@ee.bilkent.edu.tr).

Gizem Tendurus is with AB-MicroNano Inc., Bilkent University, 06800 Ankara, Turkey (e-mail: gizem.tendurus@bilkent.edu.tr).

Ekmel Ozbay is with the Nanotechnology Research Center (NANOTAM), Department of Electrical and Electronics Engineering, Institute of Materials Science and Nanotechnology (UNAM), AB-MicroNano Inc., and the Department of Physics, Bilkent University, 06800 Ankara, Turkey (e-mail: ozbay@bilkent.edu.tr).

Color versions of one or more figures in this article are available at <https://doi.org/10.1109/TED.2022.3162555>.

Digital Object Identifier 10.1109/TED.2022.3162555

electrical performance of the device, are negatively affected by increasing the channel temperature [14], [15]. As a result, the device performance deteriorates, and its mean (or median)-time-to-failure (MTF or MTTF) and reliability decline [12], [14], [16]–[18]. In order for the MTF, which is the most important quantitative indicator of device reliability, to be calculated correctly with the Arrhenius equation [3], [19], the highest temperature value called “ $T_{\max}$ ” or “hotspot” inside the device should be determined with the least possible error.  $T_{\max}$  is located below the device surface, somewhere along the channel line. The thermographic temperature measurements with IR and micro-Raman methods [20]–[22], which are widely used in remote temperature measurements, often underestimate  $T_{\max}$  due to the lack of direct optical path access to the  $T_{\max}$  point as a result of masking metal barriers on the device surface. In addition, the spatial resolution of these measurements at the  $T_{\max}$  locations in submicrometer dimensions is limited by diffraction [23]. The thermographic measurements cannot find  $T_{\max}$  alone and require additional calibrations and correlations supported by the finite element analysis (FEA) [24].

Depending on the realistic modeling of material parameters, electrical/thermal boundary conditions, thermal boundary resistances (TBRs), and device geometry, the  $T_{\max}$  value can also be calculated with a certain accuracy utilizing 2-D/3-D numerical simulations. These are 3-D electrothermal simulations, and 2-D electrothermal for electrical device simulation and 2-D/3-D thermal simulations with FEA [12], [25], [26]. The computational burden inherent in these approaches (especially in 3-D) and the need for very detailed and complex semiconductor device physics are a challenge for RF and reliability engineers in unveiling  $T_{\max}$  quickly and realistically. In some studies that do not make any electrothermal simulations, the dissipated heat distribution is usually taken as a single uniform heat source (UHS) in locations under or close to the channel [27]. In this way, 3-D FEA thermal analysis can be performed relatively quickly, but the results obtained do not give  $T_{\max}$  exactly. Moreover, the most important disadvantage of this method is that it does not consider the bias dependency for self-heating. In other words, it finds the same  $T_{\max}$  with the same total power consumption but at different current and voltage values, contrary to the physical nature and the operating conditions of the device.

In order to improve the aforementioned shortcomings, a hybrid interaction of electrical measurement and 3-D FEA is performed in the present article and the heat power distribution is modeled with a two-heat source (2HS) modeling approach [28] based on the measured output characteristics of a GaN HEMT device and considering the bias dependence of the self-heating. We demonstrate that the proposed method can find  $T_{\max}$  without the need for the electrothermal simulation but still with an accuracy close to it.

This article is organized as follows. Section II presents simulation approaches in technology computer-aided design (TCAD) and 3-D FEA thermal analysis. Also, the electrical measurement of the fabricated  $2 \times 125 \mu\text{m}$  GaN HEMT device is introduced in this section. Section III describes the method of electrical measurement-assisted 2HS

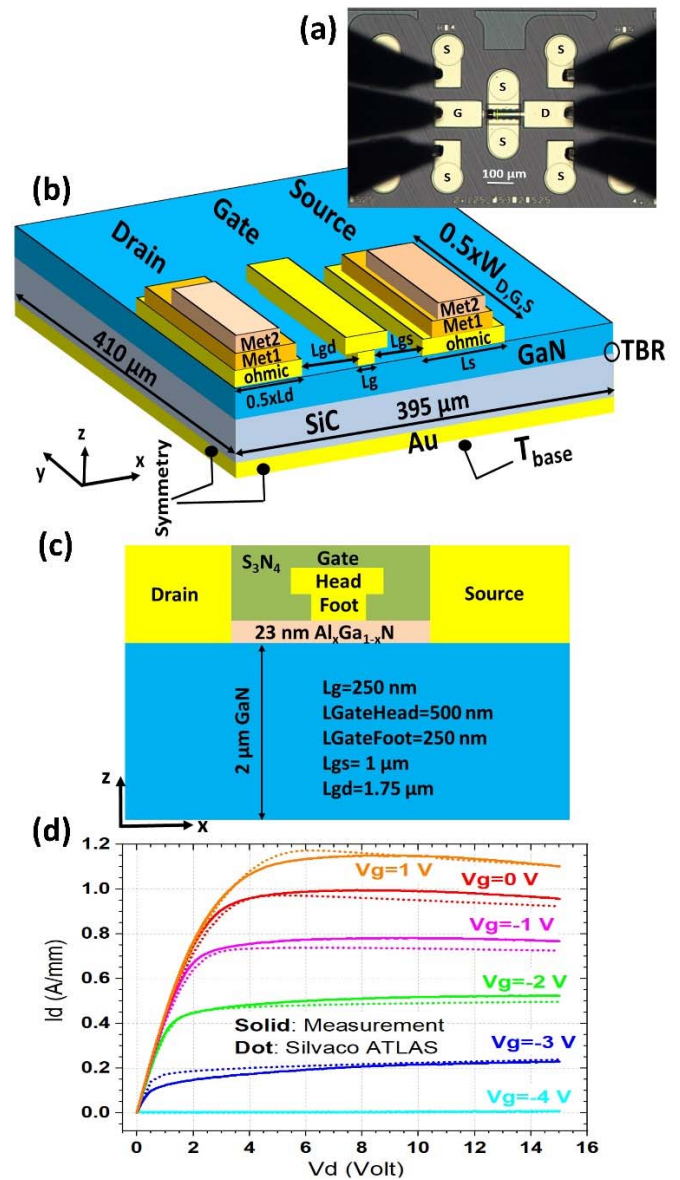
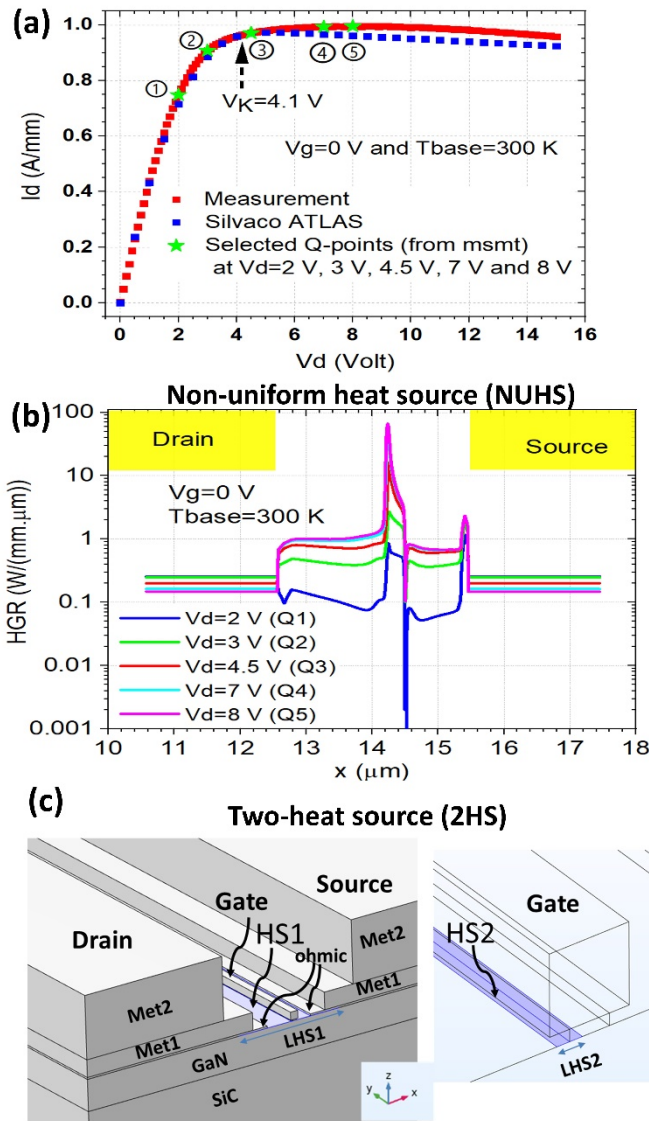


Fig. 1. (a) Photograph of the fabricated  $2 \times 125 \mu\text{m}$  GaN HEMT device with a channel length of 250 nm. [Gate (G), source (S), and drain (D) pads are labeled.] (b) 3-D finite element model of GaN HEMT device under study. (Due to the symmetry, a quarter of the device architecture is shown.) (c) 2-D TCAD electrothermal simulation layout of the device under study. (d) Output characteristics of the device at  $T_{\text{base}} = 300 \text{ K}$  using dc measurements (solid lines) and TCAD electrothermal simulations (dotted lines). The geometries in (b) and (c) are not drawn to scale.

model. Moreover, the application of the suggested method as a proof-of-concept is demonstrated and discussed in this section. The effect of the knee voltage is discussed in Section IV. Finally, Section V highlights the conclusions of the study.

## II. SIMULATION AND MEASUREMENT APPROACHES

A two-finger  $2 \times 125 \mu\text{m}$  GaN HEMT device [Fig. 1(a)] is fabricated. The 3-D quarter-symmetric architecture of the device, which we will use in the COMSOL FEA thermal simulations, is shown in Fig. 1(b). On the other hand, the 2-D view of the device in Fig. 1(c) is employed for the Silvaco



**Fig. 2.** (a) Output characteristics of the device at  $T_{\text{base}} = 300$  K and  $V_g = 0$  V using dc measurements (red colored) and TCAD electrothermal simulations (blue colored). Selected Q-points on the measurements at  $V_d = 2, 3, 4.5, 7,$  and  $8$  V are marked with green stars. Knee voltage ( $V_K$ ) is  $4.1$  V. (b) NUHS HGR profiles obtained at Q-point voltages and  $T_{\text{base}} = 300$  K by TCAD electrothermal simulations. (c) 3-D FEA thermal simulation section showing the placement of 2HSs (HS1 and HS2) in purple colored zones and their lengths ( $L_{\text{HS1}}$  and  $L_{\text{HS2}}$ ).

ATLAS TCAD electrothermal simulations that we implement to validate our proposed method. The  $300$  K isothermal at the bottom of the device and insulating boundary conditions elsewhere [Fig. 1(c)] is applied in the TCAD simulations. Temperature-dependent nonlinearity on the channel resistance and the knee voltage is included in the TCAD simulations with the electron mobility modeling approach, according to the work of Farahmand *et al.* [29]. Further details on the TCAD simulation conditions and the implementations can be found in the recent publications [10], [11] of our research group. The values of most geometric parameters of the device are presented within the 3-D and 2-D illustrations in Fig. 2(b) and (c). The thicknesses of the GaN, SiC substrate, and the

**TABLE I**  
SOURCE AND DRAIN DIMENSIONS

Dimension	Name	$\mu\text{m}$
$L_{d,\text{ohmic}}$ (or $L_d$ )	Length of ohmic layer in drain	25
$L_{d,\text{met1}}$	Length of metal 1 layer in drain	23
$L_{d,\text{met2}}$	Length of metal 2 layer in drain	19
$L_{s,\text{ohmic}}$ (or $L_s$ )	Length of ohmic layer in source	32
$L_{s,\text{met1}}$	Length of metal 1 layer in source	30
$L_{s,\text{met2}}$	Length of metal 2 layer in source	26
$W_{s,d,\text{ohmic}}$ (or $W_{s,D}$ )	Width of ohmic layer in source and drain	125
$W_{s,d,\text{met1}}$	Width of metal 1 layer in source and drain	123
$W_{d,\text{met2}}$	Width of metal 2 layer in drain	92.5
$W_{s,\text{met2}}$	Width of metal 2 layer in source	119
$t_{s,d,\text{ohmic}}$	Ohmic layer thickness in source and drain	0.12
$t_{s,d,\text{met1}}$	Thickness of metal 1 in source and drain	1.1
$t_{s,d,\text{met2}}$	Thickness of metal 2 in source and drain	4

underlying Au layer are  $2, 98,$  and  $5$   $\mu\text{m}$ , respectively. The dimensions of the metallic layers in the drain and source seen in Fig. 1(b) are given in Table I. For T-gate,  $L_{\text{GateFoot}}$  (i.e., gate length or  $L_g$ ) =  $250$  nm,  $L_{\text{GateHead}} = 500$  nm,  $W_G = 125$   $\mu\text{m}$  (for gate foot and head),  $t_{\text{GateFoot}} = 75$  nm, and  $t_{\text{GateHead}} = 500$  nm.

Although the TBR between GaN and SiC substrate varies depending on the fabrication conditions and the temperature,  $\text{TBR} = 3 \times 10^{-8}$   $\text{m}^2 \cdot \text{K} \cdot \text{W}^{-1}$ , which is widely used in the literature [30]–[32], is taken in this study. Symmetric boundary conditions on the left and front side surfaces, constant temperature ( $T_{\text{base}} = 300$  K) on the bottom surface, and adiabatic boundary conditions on all other surfaces are used in 3-D FEA thermal simulations [25], [33]. In addition, we do not use radiation and convection heat transfer mechanisms in the FEA since the heat transfer by radiation and convection is negligible compared to the conduction [33]. We use passivation ( $\text{Si}_3\text{N}_4$ ) and  $\text{Al}_x\text{Ga}_{1-x}\text{N}$  ( $x = 0.28$ ) layers in the electrothermal simulation layout in Fig. 1(c), but they are omitted in the 3-D FEA in terms of computational efficiency because their effects are negligible [33], [34]. Note that all the ohmic and metallic layers in the upper and lower regions in Fig. 1(b) are Au. In the FEA simulations, we employ the temperature-dependent thermal conductivity of the materials given in Table II. The output dc characteristics of the device at  $T_{\text{base}} = 300$  K are measured in a temperature-controlled chamber with a device analyzer/curve tracker (The Keysight Technologies, B1505A). In the same dc and temperature conditions, the output characteristic obtained by electrothermal simulation of the structure in Fig. 1(c) is in good agreement with the measurements, as shown in Fig. 1(d).

### III. ELECTRICAL MEASUREMENT-ASSISTED 2HS MODEL

We adopt the 2HS model, which was recently developed by Chen *et al.* [28] in which the dissipated thermal power

TABLE II  
THERMAL CONDUCTIVITIES UTILIZED IN THE FEA SIMULATIONS

Material	Temperature (K)	Thermal conductivity (W/m.K)
GaN [33], [35]	$T$	$150 \times (300/T)^{1.4}$
SiC [33], [35]	$T$	$387 \times (293/T)^{1.49}$
Au [36]	100	327
	200	323
	400	311
	600	298
	800	284
	1000	270

data required for the 2HS model are obtained from the output  $I$ - $V$  plot based on the TCAD simulations. Unlike their work, we will apply the 2HS model using the measurement  $I$ - $V$  plot to benefit directly and quickly from the electrical measurements of the device under consideration. Accordingly, we select five operating quiescent ( $Q$ ) points indicated by green stars on the dc measurement graph [Fig. 2(a)] at  $T_{\text{base}} = 300$  K and  $V_g = 0$  V conditions. For  $I$ - $V$  measurement graph at  $V_g = 0$  V, we take the knee voltage ( $V_K$ ) 4.1 V. In this case, the selected  $Q$ -points of 1 and 2 ( $V_d = 2$  and 3 V) take place in the linear regime and 3–5 ( $V_d = 4.5, 7,$  and 8 V) are in the saturation regime. According to the 2HS model, the details of which were explained in the previous study [28], we distribute the total dissipated power ( $P = V_d \times I_d$ ) of the device to the 2HS regions (HS1 and HS2) as  $P_1$  and  $P_2$  such that  $P = P_1 + P_2$ . When the device is in the linear regime at  $V_d \leq V_K$ , all the power is converted to heat in the HS1 region ( $P_1 = V_d \times I_d$ ), while no heat is consumed in the HS2 region ( $P_2 = 0$ ). When the device is in the saturation regime at  $V_d > V_K$ ,  $P_1 = V_K \times I_d$ , and  $P_2 = (V_d - V_K) \times I_d$ . These heat sources are applied to the purple areas on the GaN layer as the surface heat generation rate (HGR) with a width of  $W = 125 \mu\text{m}$  and lengths of  $L_{\text{HS1}}$  and  $L_{\text{HS2}}$ , as shown in the 3-D FEA section in Fig. 2(c). Here,  $L_{\text{HS1}} = 2 \mu\text{m} + L_{\text{gd}} + L_g + L_{\text{gs}} + 2 \mu\text{m}$  where heat loss up to  $2 \mu\text{m}$  transfer lengths is taken under drain and source ohmic metallizations. As in the previous work [28], we opt for  $L_{\text{HS2}} = 160$  nm to represent the length of the high electric field region and centered around the gate edge on the drain side, assuming that this is independent of the device geometry. On the other hand, we calculate the non-UHS (NUHS) distribution at the corresponding  $Q$ -points in the TCAD  $I$ - $V$  plot in Fig. 2(a), which we calibrated by the measurement. Then, we perform FEA by applying the NUHSs in Fig. 2(b) along  $L_{\text{HS1}}$  in Fig. 2(c) as HGRs to validate the proposed 2HS method. The HGR profiles under NUHS in Fig. 2(b) also illustrate quite well the two main heat generation mechanisms that we model in the 2HS approach above. The first type is related to the drain and source access regions. This type is similar to HS1 in the 2HS and valid in the linear regime under low electric field cases. The second type is related to gate edge on the drain-side region. This type is similar to HS2

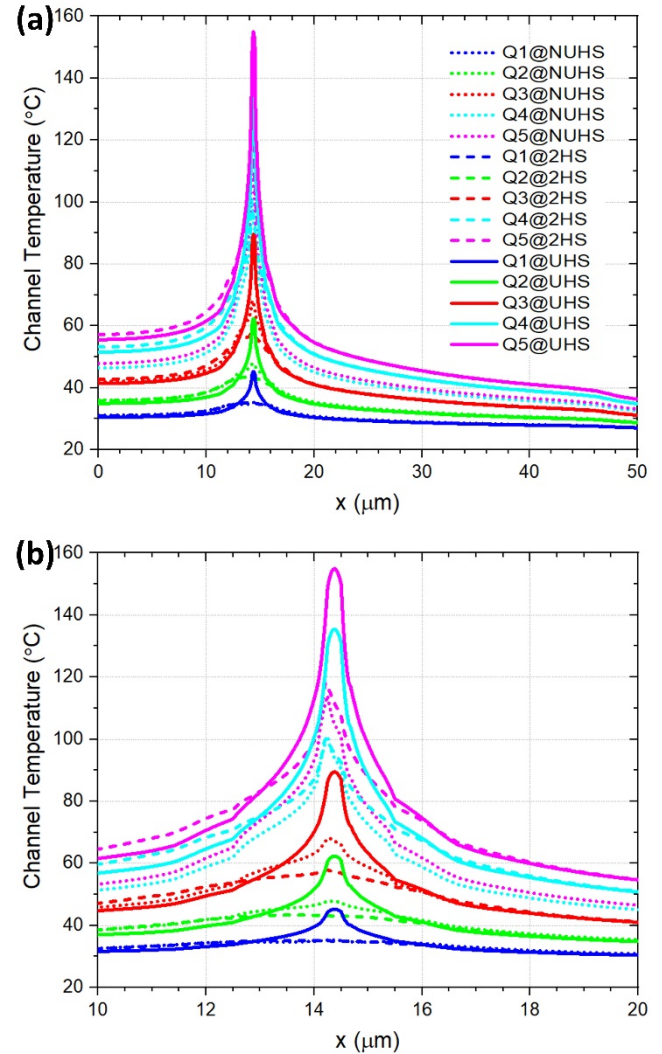


Fig. 3. (a) Temperature profiles along the channel at  $Q$ -points obtained by NUHS, 2HS, and UHS methods, indicated by dotted, dashed, and solid lines, respectively. (b) Zooming in the temperature profile of (a) at  $x = 10$ – $20 \mu\text{m}$ . In all the methods here,  $T_{\text{base}} = 300$  K and  $V_g = 0$  V. In 2HS,  $V_K = 4.1$  V and  $L_{\text{HS2}} = 0.16 \mu\text{m}$ .

in the 2HS and valid in the saturation regime under the higher electric field cases.

In addition to representing heat with 2HS and NUHS, we also implement UHS modeling in the FEA, which is often preferred because of its simplicity in thermal analysis. In the FEA with UHS approach, the constant powers obtained at the measurement  $Q$ -points (1.5, 2.7, 4.4, 7, and 8 W/mm) are applied just under the gate foot electrode as fixed HGRs with a length of  $L_g = 250$  nm. Therefore, the temperature profiles along the channel at  $T_{\text{base}} = 300$  K and  $V_g = 0$  V are obtained with different heat modeling approaches. They are shown in Fig. 3 comparatively. It is clearly seen that the  $T_{\text{max}}$  values in the UHS method are not only overestimated compared to the other two methods, but their positions are slightly shifted toward the positive  $x$ -direction. On the other hand, with the proposed 2HS method, it is seen that the temperature profiles at different points are quite compatible with the electrothermal simulation results in terms of both  $T_{\text{max}}$  values and locations.

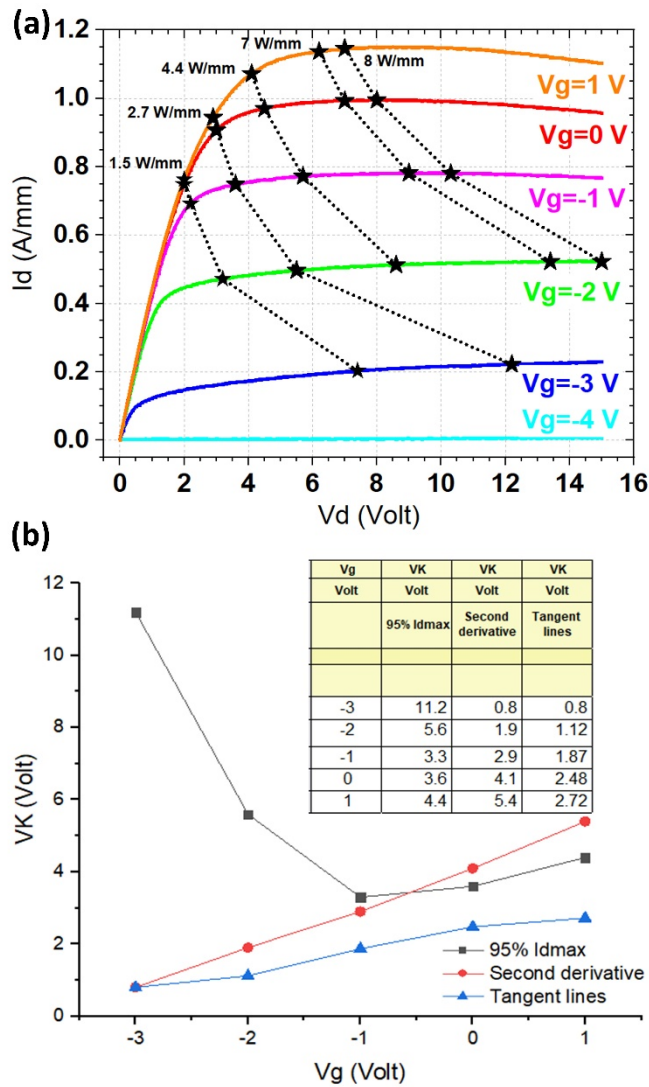


Fig. 4. (a) Output characteristics of the device at  $T_{\text{base}} = 300$  K using dc measurements. The constant powers of the Q-points at  $V_g = 0$  V (1.5, 2.7, 4.4, 7, and 8 W/mm) are mapped to the output plots at the other  $V_g$ 's and shown with black stars and dotted lines. (b) Knee voltage ( $V_K$ ) graph calculated according to three different methods at varying gate voltages ( $V_g$ ). The inset presents the corresponding numerical values in tabular form.

#### IV. EFFECT OF KNEE VOLTAGE

To show that our method also works at the gate voltages other than  $V_g = 0$  V, we map the constant power points to other  $V_g$  curves as in Fig. 4(a) in a manner that maintains constant powers that are marked as black stars. Since the heat allocation to the two zones in the 2HS method is made according to  $V_K$ , it is important to determine  $V_K$  correctly from the output  $I-V$  graph. We utilize three different techniques to find  $V_K$ . These are “95%  $I_{\text{dmax}}$ ,” “second derivative,” and “tangent lines.” As the name suggests, the first technique considers the drain voltage as knee voltage, corresponding to 95% of the maximum drain current at a fixed gate bias. If the measured output  $I-V$  at any  $V_g$  has a nonmonotonic characteristic such that it reaches the peak value of  $I_d$  (i.e.,  $I_{\text{dmax}}$ ) within the measurement interval of  $V_d$  and then decreases with increasing

$V_d$ , then the knee voltages found by this technique are close to reality (e.g.,  $V_g = -1, 0$ , and  $1$  V cases in Fig. 4). Otherwise, in a monotonically increasing  $I-V$  graph with  $V_d$ , the real peak current cannot be reached in the measurement range, so the knee voltages obtained with this technique may not be realistic (e.g.,  $V_g = -3$  and  $-2$  V cases in Fig. 4). In the “second derivative” method, a special function  $G = (\partial/\partial V_d)(\partial I_d/\partial V_d)^{-1}$  is computed from the measured output  $I-V$  data at a fixed  $V_g$ , and  $V_K$  is extracted from the peak observed points in the  $G$  versus  $V_d$  plot [37], [38]. In the “tangent lines” technique, the knee voltage is found from the intersection point of the two tangent curves drawn to the measured  $I-V$  graph at the minimum and maximum drain voltages within the measurement range. Fig. 4(b) shows the knee voltages resulting from applying these techniques on the  $I-V$  graphs from  $V_g = -3$  to  $1$  V. We repeat the 2HS method at the selected fixed power Q-points with different knee voltages found in the  $V_g = -3, -2, -1, 0$ , and  $1$  V curves at  $T_{\text{base}} = 300$  K. Next, we compare the 2HS results with the channel temperature profiles found by the NUHS method in a manner similar to Fig. 3. In general, depending on the correct determination of the knee voltage, it is observed that the 2HS method can uncover the channel temperature profile and  $T_{\max}$  close to the electrothermal simulation values at different bias conditions.

#### V. CONCLUSION

We have demonstrated that  $T_{\max}$  can be determined quickly and close to the electrothermal simulations in a GaN HEMT device with a 2HS method and FEA hybrid interaction, supported by electrical output measurements of the device under various bias conditions. In addition, the dependence of the method on the knee voltage and its accurate determination has also been thoroughly investigated with different knee-detection techniques. The suggested method provides an easy-to-implement alternative to reveal the hotspot location and value, which is essential for GaN HEMT reliability engineering.

#### ACKNOWLEDGMENT

The authors would like to thank all the members of the Nanotechnology Research Center (NANOTAM) and ABMN Gallium Nitride (GaN) Fabrication, RF Design, Reliability, and Research and Development Groups.

#### REFERENCES

- [1] U. K. Mishra, P. Parikh, and Y.-F. Wu, “AlGaIn/GaN HEMTs—an overview of device operation and applications,” *Proc. IEEE*, vol. 90, no. 6, pp. 1022–1031, Jun. 2002, doi: [10.1109/JPROC.2002.1021567](https://doi.org/10.1109/JPROC.2002.1021567).
- [2] H. Amano *et al.*, “The 2018 GaN power electronics roadmap—IOPscience,” *J. Phys. D, Appl. Phys.*, vol. 51, no. 6, 2018, Art. no. 163001. [Online]. Available: <https://iopscience.iop.org/article/10.1088/1361-6463/aaaf9d%0Ahttps://iopscience.iop.org/article/10.1088/1361-6463/aaaf9d/meta>
- [3] F. Roccaforte and M. Leszczynski, Eds., *Nitride Semiconductor Technology*. Hoboken, NJ, USA: Wiley, 2020.
- [4] J. He, W. C. Cheng, Q. Wang, K. Cheng, H. Yu, and Y. Chai, “Recent advances in GaN-based power HEMT devices,” *Adv. Electron. Mater.*, vol. 7, no. 4, pp. 1–24, 2021, doi: [10.1002/aelm.202001045](https://doi.org/10.1002/aelm.202001045).

- [5] B. S. Sengar, A. Kumar, M. Reddeppa, S. Kumar, and H. N. Oo, "GaN-based technology for 5G applications," in *CMOS Analog IC Design for 5G Beyond*. Cham, Switzerland: Springer, 2021, pp. 147–155.
- [6] K. H. Teo *et al.*, "Emerging GaN technologies for power, RF, digital, and quantum computing applications: Recent advances and prospects," *J. Appl. Phys.*, vol. 130, no. 16, Oct. 2021, Art. no. 160902, doi: [10.1063/5.0061555](https://doi.org/10.1063/5.0061555).
- [7] K. Husna Hamza and D. Nirmal, "A review of GaN HEMT broadband power amplifiers," *AEU Int. J. Electron. Commun.*, vol. 116, Mar. 2020, Art. no. 153040, doi: [10.1016/j.aeue.2019.153040](https://doi.org/10.1016/j.aeue.2019.153040).
- [8] J. Scarpulla, "Guidelines for space qualification of GaN HEMTs and MMICs," in *Proc. IEEE Int. Rel. Phys. Symp. (IRPS)*, Mar. 2021, pp. 1–11, doi: [10.1109/IRPS46558.2021.9405226](https://doi.org/10.1109/IRPS46558.2021.9405226).
- [9] J. Millan, P. Godignon, X. Perpina, A. Perez-Tomas, and J. Rebollo, "A survey of wide bandgap power semiconductor devices," *IEEE Trans. Power Electron.*, vol. 29, no. 5, pp. 2155–2163, May 2014, doi: [10.1109/TPEL.2013.2268900](https://doi.org/10.1109/TPEL.2013.2268900).
- [10] O. Odabasi, M. O. Akar, B. Butun, and E. Ozbay, "Improved  $T_{MAX}$  estimation in GaN HEMTs using an equivalent hot point approximation," *IEEE Trans. Electron Devices*, vol. 67, no. 4, pp. 1553–1559, Apr. 2020, doi: [10.1109/TED.2020.2976030](https://doi.org/10.1109/TED.2020.2976030).
- [11] O. Odabasi, B. Bütün, and E. Özbay, "Realistic channel temperature simulation of AlGaIn/GaN high electron mobility transistors," in *Proc. Eur. Microw. Conf. Central Eur. (EuMCE)*, May 2019, pp. 87–90.
- [12] X. Chen, S. Boumaiza, and L. Wei, "Self-heating and equivalent channel temperature in short gate length GaN HEMTs," *IEEE Trans. Electron Devices*, vol. 66, no. 9, pp. 3748–3755, Sep. 2019, doi: [10.1109/TED.2019.2926742](https://doi.org/10.1109/TED.2019.2926742).
- [13] R. J. Warzoha *et al.*, "Applications and impacts of nanoscale thermal transport in electronics packaging," *J. Electron. Packag.*, vol. 143, no. 2, Jun. 2021, Art. no. 020804, doi: [10.1115/1.4049293](https://doi.org/10.1115/1.4049293).
- [14] D. J. Cheney *et al.*, "Reliability studies of AlGaIn/GaN high electron mobility transistors," *Semiconductor Sci. Technol.*, vol. 28, no. 7, Jul. 2013, Art. no. 074019, doi: [10.1088/0268-1242/28/7/074019](https://doi.org/10.1088/0268-1242/28/7/074019).
- [15] M. Meneghini *et al.*, "GaN-based power devices: Physics, reliability and perspectives," *J. Appl. Phys.*, vol. 130, no. 16, p. 227, 2021, doi: [10.1063/5.0061354](https://doi.org/10.1063/5.0061354).
- [16] J. A. del Alamo and J. Joh, "GaN HEMT reliability," *Microelectron. Rel.*, vol. 49, no. 9, pp. 1200–1206, Sep. 2009, doi: [10.1016/j.microrel.2009.07.003](https://doi.org/10.1016/j.microrel.2009.07.003).
- [17] B. M. Paine, S. R. Polmanter, V. T. Ng, N. T. Kubota, and C. R. Ignacio, "Lifetesting GaN HEMTs with multiple degradation mechanisms," *IEEE Trans. Device Mater. Rel.*, vol. 15, no. 4, pp. 486–494, Dec. 2015, doi: [10.1109/TDMR.2015.2474359](https://doi.org/10.1109/TDMR.2015.2474359).
- [18] S. Li, Z. Chen, Q. Liu, W. Shi, and K. Li, "Modeling and analysis of performance degradation data for reliability assessment: A review," *IEEE Access*, vol. 8, pp. 74648–74678, 2020, doi: [10.1109/ACCESS.2020.2987332](https://doi.org/10.1109/ACCESS.2020.2987332).
- [19] A. M. Darwish, H. A. Hung, and A. A. Ibrahim, "AlGaIn/GaN HEMT with distributed gate for channel temperature reduction," *IEEE Trans. Microw. Theory Techn.*, vol. 60, no. 4, pp. 1038–1043, Apr. 2012, doi: [10.1109/TMTT.2012.2185948](https://doi.org/10.1109/TMTT.2012.2185948).
- [20] M. Kuball and J. W. Pomeroy, "A review of Raman thermography for electronic and opto-electronic device measurement with sub-micron spatial and nanosecond temporal resolution," *IEEE Trans. Device Mater. Rel.*, vol. 16, no. 4, pp. 667–684, Dec. 2016, doi: [10.1109/TDMR.2016.2617458](https://doi.org/10.1109/TDMR.2016.2617458).
- [21] A. Sarua *et al.*, "Integrated micro-Raman/infrared thermography probe for monitoring of self-heating in AlGaIn/GaN transistor structures," *IEEE Trans. Electron Devices*, vol. 53, no. 10, pp. 2438–2447, Oct. 2006, doi: [10.1109/TED.2006.882274](https://doi.org/10.1109/TED.2006.882274).
- [22] B. Öner, J. W. Pomeroy, and M. Kuball, "Submicrometer resolution hyperspectral quantum rod thermal imaging of microelectronic devices," *ACS Appl. Electron. Mater.*, vol. 2, no. 1, pp. 93–102, Jan. 2020, doi: [10.1021/acsaelm.9b00575](https://doi.org/10.1021/acsaelm.9b00575).
- [23] J. S. Lundh *et al.*, "2D materials for universal thermal imaging of micro- and nanodevices: An application to gallium oxide electronics," *ACS Appl. Electron. Mater.*, vol. 2, no. 9, pp. 2945–2953, Sep. 2020, doi: [10.1021/acsaelm.0c00574](https://doi.org/10.1021/acsaelm.0c00574).
- [24] Y. Durna, H. Kocer, Y. E. Aras, M. C. Soydan, B. Butun, and E. Ozbay, "Correlation-based study of FEA and IR thermography to reveal the 2DEG temperature of a multi-fingered high-power GaN HEMT," *J. Appl. Phys.*, vol. 131, no. 8, Feb. 2022, Art. no. 085107, doi: [10.1063/5.0084511](https://doi.org/10.1063/5.0084511).
- [25] F. Bertoluzza, N. Delmonte, and R. Menozzi, "Three-dimensional finite-element thermal simulation of GaN-based HEMTs," *Microelectron. Rel.*, vol. 49, no. 5, pp. 468–473, May 2009, doi: [10.1016/j.microrel.2009.02.009](https://doi.org/10.1016/j.microrel.2009.02.009).
- [26] T. Gerrer *et al.*, "Thermal design rules of AlGaIn/GaN-based microwave transistors on diamond," *IEEE Trans. Electron Devices*, vol. 68, no. 4, pp. 1530–1536, Apr. 2021, doi: [10.1109/TED.2021.3061319](https://doi.org/10.1109/TED.2021.3061319).
- [27] E. A. Douglas, F. Ren, and S. J. Pearton, "Finite-element simulations of the effect of device design on channel temperature for AlGaIn/GaN high electron mobility transistors," *J. Vac. Sci. Technol. B, Nanotechnol. Microelectron., Mater., Process., Meas., Phenomena*, vol. 29, no. 2, Mar. 2011, Art. no. 020603, doi: [10.1116/1.3567183](https://doi.org/10.1116/1.3567183).
- [28] X. Chen, S. Boumaiza, and L. Wei, "Modeling bias dependence of self-heating in GaN HEMTs using two heat sources," *IEEE Trans. Electron Devices*, vol. 67, no. 8, pp. 3082–3087, Aug. 2020, doi: [10.1109/TED.2020.3003847](https://doi.org/10.1109/TED.2020.3003847).
- [29] M. Farahmand *et al.*, "Monte Carlo simulation of electron transport in the III-nitride Wurtzite phase materials system: Binaries and ternaries," *IEEE Trans. Electron Devices*, vol. 48, no. 3, pp. 535–542, Mar. 2001, doi: [10.1109/16.906448](https://doi.org/10.1109/16.906448).
- [30] A. Manoi, J. W. Pomeroy, N. Killat, and M. Kuball, "Benchmarking of thermal boundary resistance in AlGaIn/GaN HEMTs on SiC substrates: Implications of the nucleation layer microstructure," *IEEE Electron Device Lett.*, vol. 31, no. 12, pp. 1395–1397, Dec. 2010, doi: [10.1109/LED.2010.2077730](https://doi.org/10.1109/LED.2010.2077730).
- [31] K. Park and C. Bayram, "Thermal resistance optimization of GaN/substrate stacks considering thermal boundary resistance and temperature-dependent thermal conductivity," *Appl. Phys. Lett.*, vol. 109, no. 15, pp. 1–5, 2016, doi: [10.1063/1.4964711](https://doi.org/10.1063/1.4964711).
- [32] Y. Feng *et al.*, "High quality GaN-on-SiC with low thermal boundary resistance by employing an ultrathin AlGaIn buffer layer," *Appl. Phys. Lett.*, vol. 118, no. 5, 2021, Art. no. 052104, doi: [10.1063/5.0037796](https://doi.org/10.1063/5.0037796).
- [33] M. Azarifar and N. Donmez, "A roadmap for building thermal models for AlGaIn/GaN HEMTs: Simplifications and beyond," in *Proc. ASME Summer Heat Transf. Conf.*, Jul. 2016, pp. 1–7.
- [34] K. R. Bagnall, *Device-Level Thermal Analysis of GaN-Based Electronics*. Cambridge, MA, USA: Massachusetts Institute of Technology, 2013.
- [35] X. Chen, F. N. Donmez, S. Kumar, and S. Graham, "A numerical study on comparing the active and passive cooling of AlGaIn/GaN HEMTs," *IEEE Trans. Electron Devices*, vol. 61, no. 12, pp. 4056–4061, Dec. 2014, doi: [10.1109/TED.2014.2360504](https://doi.org/10.1109/TED.2014.2360504).
- [36] Y. A. Çengel and A. J. Ghajar, *Heat and Mass Transfer: Fundamentals & Applications*, 5th ed. New York, NY, USA: McGraw-Hill, 2015.
- [37] W.-Y. Jang, C.-Y. Wu, and H.-J. Wu, "A new experimental method to determine the saturation voltage of a small-geometry MOSFET," *Solid State Electron.*, vol. 31, no. 9, pp. 1421–1431, Sep. 1988, doi: [10.1016/0038-1101\(88\)90108-6](https://doi.org/10.1016/0038-1101(88)90108-6).
- [38] R. Picos, M. Roca, B. Iñiguez, and E. García-Moreno, "Improved direct determination of MOSFET saturation voltage using Fourier techniques," *IEEE Trans. Electron Devices*, vol. 51, no. 12, pp. 2073–2077, Dec. 2004, doi: [10.1109/TED.2004.838317](https://doi.org/10.1109/TED.2004.838317).